TOMOGRAPHY

P. F. Worcester, University of California at San Diego, La Jolla, CA, USA

doi:10.1006/rwos.2001.0310

Introduction

Ocean acoustic tomography is a method for acoustic remote sensing of the ocean interior that takes advantage of the facts that the propagation of sound through the ocean is sensitive to quantities of oceanographic interest, such as temperature and water velocity, and that the ocean is nearly transparent to low-frequency sound so that signals can be transmitted over long distances. The procedure is (i) to transmit acoustic signals through the ocean, (ii) to make precise measurements of the properties of the received signals, e.g., travel times, and (iii) to use inverse methods to infer the state of the ocean traversed by the sound field from the measured properties. The characteristics of the ocean between the sources and receivers are determined, rather than the characteristics of the ocean at the instruments as is the case for conventional thermometers and current meters.

Ocean acoustic tomography has a number of attractive attributes. It makes possible the rapid and repeated measurement of ocean properties over large areas, taking advantage of the speed with which sound travels in water ($\sim 1500\,\mathrm{m\,s^{-1}}$). It permits the monitoring of regions in which it is difficult to install instruments to make direct measurements, such as the Gulf Stream or the Strait of Gibraltar, using sources and receivers on the periphery of the region. Acoustic measurements are inherently spatially integrating, suppressing the small-scale variability that can contaminate point measurements and providing direct measurements of horizontal and vertical averages over large ranges. Finally, the amount of data grows as the product $(S \times R)$ of the number of acoustic sources S and receivers R, rather than linearly as the sum of the number of instruments $(S + R)$ as is the case for point measurements.

Ocean acoustic tomography was originally introduced by Munk and Wunsch in 1979 to address the difficult problem of observing the evolving ocean mesoscale. Mesoscale variability has spatial scales of order 100 km and timescales of order one month. The short timescales mean that ships move too slowly for ship-based measurements to be practical. The short spatial scales mean that moored sensors must be too closely spaced to be practical. Munk and Wunsch proposed that the travel times of acoustic signals propagating between a relatively small number of sources and receivers could be used to map the evolving temperature field in the intervening ocean. Their work led directly to the first 3D ocean acoustic tomography experiment, conducted in 1981. In spite of the marginal acoustic sources that were available at the time, the experiment showed that it was possible to use acoustic methods to map the evolving mesoscale field in a 300 km by 300 km region (**Figure 1**).

It was quickly realized, however, that the integral measures provided by acoustic methods are powerful tools for addressing certain types of problems, including the measurement of integral quantities such as heat content, mass transport, and circulation. Acoustic measurements of the integrated water velocity around a closed contour, for example, provide the circulation, which is directly related to the areal-average vorticity in the interior by Stokes' theorem. Vorticity is difficult to measure in other ways. The suppression of small-scale variability in the spatially integrating acoustic measurements also makes them well suited to measure large-scale phenomena, such as the barotropic and baroclinic tides. Finally, the integral measurements provided by the acoustic data can be used to test the skill of dynamic models and to provide strong model constraints.

Acoustic scattering due to small-scale oceanic variability (e.g., internal waves) causes the properties of the received acoustic signals to fluctuate. Although these fluctuations limit the precision with which the signal characteristics can be measured and with which oceanic parameters such as temperature and water velocity can be inferred, it was soon realized that measurements of the statistics of the fluctuations can be used to infer the statistical properties of the small-scale oceanic variability, such as internal-wave energy level, as a function of space and time.

Summarizing, tomographic methods can be used to map the evolving ocean, to provide integral measures of its properties, and to characterize the statistical behavior of small-scale oceanic variability.

Ocean Acoustics: The Forward Problem

The 'forward' problem in ocean acoustics is to compute the properties of the received signal given the

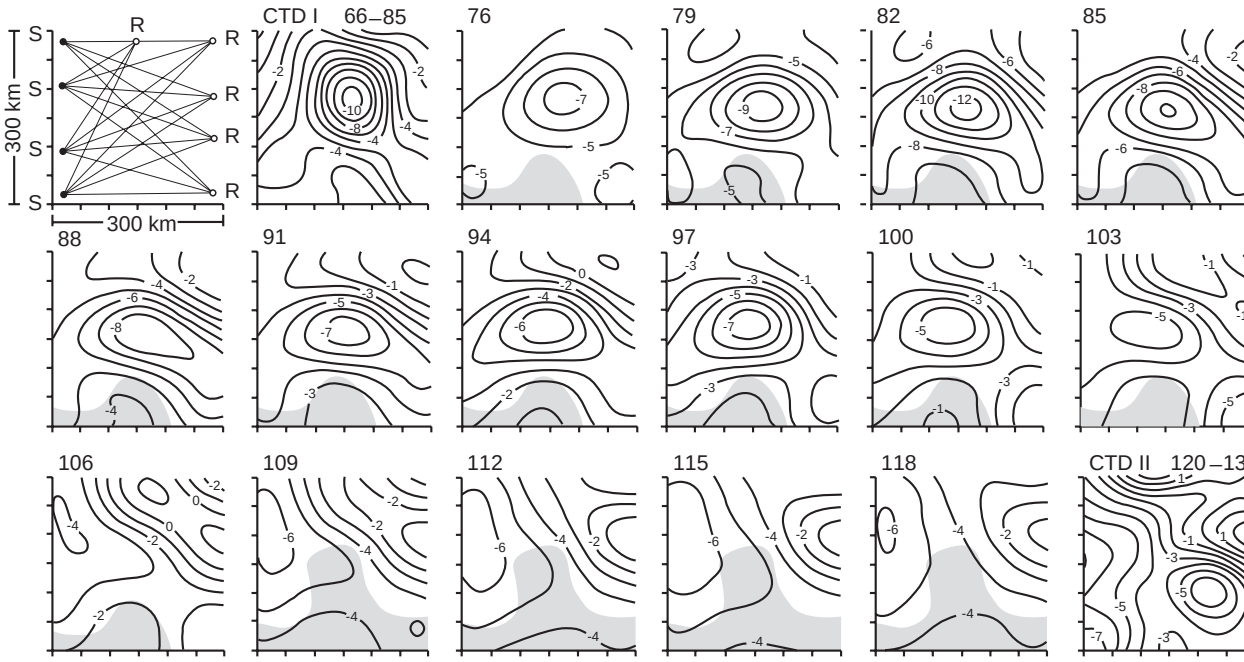

Figure 1 The 1981 tomography experiment. The first panel shows the geometry, with four source (S) and five receiver (R) moorings on the periphery of a 300 km by 300 km region in the north-west Atlantic Ocean. Subsequent panels show the sound-speed perturbations at 700 m depth derived from the acoustic data at 3-day intervals, with regions of high uncertainty shaded. The initial and final panels are derived from two ship-borne conductivity-temperature-depth (CTD) surveys, each of which required about 20 days to complete. The label on each panel is the year day in 1981. The contour interval is $1\,\mathrm{m\,s^{-1}}$ (0.2°C). Adapted from Cornuelle B, Wunsch C, Behringer D, *et al.* (1985) Tomographic maps of the ocean mesoscale. Part I: Pure acoustics. *Journal of Physical Oceanography* 15: 133–152.

sound-speed $C(x, y, z)$ and current $\mathbf{v}(x, y, z)$ fields between the source and receiver. Acoustic remote sensing of the ocean interior requires first a full understanding of the forward problem, i.e., of methods for finding solutions to the wave equation. A variety of approaches are available to do this, including geometric optics, normal mode, and parabolic equation methods. The appropriate method depends in part on the character of the sound-speed and current fields (e.g., range-independent or range-dependent) and in part on the choice of the observables in the received signal to use in the inverse problem.

The approach most commonly used in ocean acoustic tomography has been to transmit broadband signals designed to measure the impulse response of the ocean channel and to interpret the peaks in the impulse response in terms of geometric rays. Ray travel times are robust observables in the presence of internal-wave-induced scattering because of Fermat's principle, which states that ray travel times are not sensitive to first-order changes in the ray path. Other observables are possible, however. The peaks in the impulse response are in some cases more appropriately interpreted in terms of normal-mode arrivals, for example, and the observables are then modal group delays. Another possibility is to perform full-field inversions that use the time series of intensity and phase for the entire received signal as observables. Unfortunately, neither normal modes nor the intensities and phases of the received signal are robust in the presence of internal-wave-induced scattering, and so tend to be useful only at short ranges and/or low frequencies where internal-wave-induced scattering is less important. A number of other possible observables have been proposed as well. In what follows the use of ray travel times as observables will be emphasized, in part because they have been the observable most commonly used to date and in part because they are robust to internal-wave-induced scattering.

Ocean Sound Channel

The speed with which sound travels in the ocean increases with increasing temperature, salinity, and pressure. As a result, over much of the temperate world ocean there is a subsurface minimum in sound speed at depths of roughly 1000 m. Sound speed increases toward the surface above the minimum because of increasing temperature and toward the bottom below the minimum because of increasing pressure. Salinity does not play a major role

because its effect on sound speed is normally less than that of either temperature or pressure. The depth of the sound-speed minimum is called the sound channel axis. The axis shoals towards high latitudes where the surface waters are colder, actually reaching the surface during winter at sufficiently high latitudes.

The sound speed gradients above and below the sound channel axis refract acoustic rays toward the axis in accord with Snell's law. Near-horizontal rays propagating outward from an omnidirectional source on the axis will therefore tend to be trapped, cycling first above and then below the axis (**Figure 2**). Such rays are referred to as refracted–refracted (RR) rays. Steeper rays will interact with the surface and/or seafloor. Rays can reflect from the sea surface with relatively low loss. Rays that are refracted at depth and reflected from the sea surface are referred to as refracted-surface-reflected (RSR) rays. Both RR and RSR rays can propagate to long distances and are commonly used in ocean acoustic tomography. Rays that interact with the seafloor tend to be strongly scattered, however. Rays with multiple bottom interactions therefore tend not to propagate to long ranges.

A receiver at a specified range from an omnidirectional acoustic source will detect a discrete set of ray arrivals (**Figure 2**), corresponding to the rays that are at the depth of the receiver at the appropriate range. These rays are called eigenrays and are

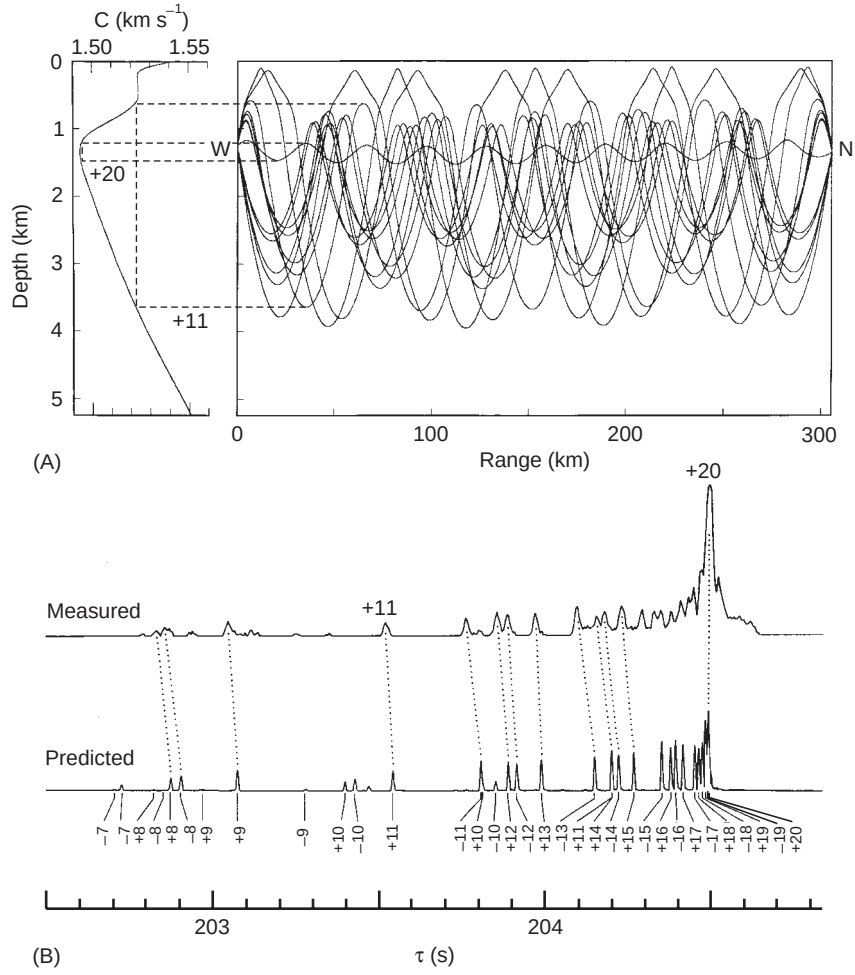

Figure 2 (A) Sound-speed profile in the western North Atlantic and the corresponding ray paths for source and receiver near the depth of the sound channel axis and about 300 km apart. The geometry is that of a reciprocal acoustic transmission experiment conducted in 1983 with transceivers designated W(est) and N(orth). (B) Measured and predicted acoustic amplitudes as a function of time for the 1983 experiment. The arrivals are labeled with their ray identifier. The earliest arrivals are from steep ray paths that cycle through nearly the entire water column. The latest arrivals are from flat ray paths that remain near the sound-channel axis. The differences between the measured and predicted arrival times are the data used in tomographic inversions. Adapted from Howe BM, Worcester PF and Spindel RC (1987) Ocean acoustic tomography: mesoscale velocity. *Journal of Geophysical Research* 92: 3785–3805.

designated $\pm p$, where $\pm$ indicates an upward/downward launch direction and p is the total number of ray turning points (including reflections). The ray geometry controls the vertical sampling properties of tomographic measurements. One can obtain significant vertical resolution even for the case of source and receiver both on the sound channel axis, because the eigenrays in general have a range of turning depths.

Ray Travel Time

To first order in $|\mathbf{v}|/C$, the travel time τ_i of ray i is

$$\tau_i = \int_{\Gamma_i} \frac{ds}{C(\mathbf{r}) + \mathbf{v}(\mathbf{r}) \cdot \mathbf{r}'} \qquad [1]$$

where Γ_i is the ray path for ray i along which distance s is measured and $\mathbf{r}'$ is the tangent to the ray at position $\mathbf{r}$. The sign of $\mathbf{v} \cdot \mathbf{r}'$ depends on the direction of propagation, and the travel times and ray paths in opposite directions differ because of the effects of currents. (Sound travels faster with a current than against a current.) The eigenrays Γ_i are obtained using a numerical eigenray code.

The Inverse Problem

The 'inverse' problem is to compute the sound-speed $C(\mathbf{r})$ and current $\mathbf{v}(\mathbf{r})$ fields given the measured travel times. In fact, a great deal is normally known about $C(\mathbf{r})$ in the ocean from climatological or other data. The interesting problem is therefore to compute the perturbations from an assumed reference state, using the measured perturbations from the travel times computed for the reference state.

Data

Travel times are in general a nonlinear function of the sound-speed and current fields, because the ray path Γ_i depends on $C(\mathbf{r})$ and $\mathbf{v}(\mathbf{r})$. Linearize by setting

$$C(\mathbf{r}) = C(\mathbf{r}, -) + \Delta C(\mathbf{r}) \qquad [2]$$

$$\mathbf{v}(\mathbf{r}) = \mathbf{v}(\mathbf{r}, -) + \Delta \mathbf{v}(\mathbf{r}) \qquad [3]$$

where $C(\mathbf{r}, -), \mathbf{v}(\mathbf{r}, -)$ are the known reference states. The argument $(-)$ denotes the dependence of the variables only on the reference state, independent of the measurements. Normally,

$$|\Delta C(\mathbf{r})| \ll C(\mathbf{r}, -) \qquad [4]$$

$$|\Delta \mathbf{v}(\mathbf{r})| \ll C(\mathbf{r}, -) \qquad [5]$$

In general, however,

$$|\Delta \mathbf{v}(\mathbf{r})| > |\mathbf{v}(\mathbf{r}, -)| \qquad [6]$$

because the fluctuations in current at a fixed location in the ocean are typically large compared to the time-mean current.

Setting $\mathbf{v}(\mathbf{r}, -) \equiv 0, \Delta \mathbf{v}(\mathbf{r}) \equiv \mathbf{v}(\mathbf{r})$, forming perturbation travel times, and linearizing to first order in $\Delta C/C$ and $|\mathbf{v}|/C$ gives

$$\Delta\tau_i^+ = \tau_i^+ - \tau_i(-) = -\int_{\Gamma_{i(-)}} \frac{[\Delta C(\mathbf{r}) + \mathbf{v}(\mathbf{r}) \cdot \mathbf{r}'(-)]}{C^2(\mathbf{r}, -)}\, ds \qquad [7]$$

$$\Delta\tau_i^- = \tau_i^- - \tau_i(-) = -\int_{\Gamma_{i(-)}} \frac{[\Delta C(\mathbf{r}) - \mathbf{v}(\mathbf{r}) \cdot \mathbf{r}'(-)]}{C^2(\mathbf{r}, -)}\, ds \qquad [8]$$

where $\Gamma_{i(-)}, \mathbf{r}'(-)$ are the ray path and tangent vector for the reference state. The superscript plus (minus) refers to propagation in the $+(-)$ direction. The reference travel time is

$$\tau_i(-) = \int_{\Gamma_{i(-)}} \frac{ds}{C(\mathbf{r}, -)} \qquad [9]$$

The sum of the travel time perturbations

$$\Delta s_i = \frac{1}{2}(\Delta\tau_i^+ + \Delta\tau_i^-) = -\int_{\Gamma_{i(-)}} \frac{ds}{C^2(\mathbf{r}, -)} \Delta C(\mathbf{r}) \qquad [10]$$

depends only on the sound-speed perturbation $\Delta C(\mathbf{r})$. The difference

$$\Delta d_i = \frac{1}{2}(\Delta\tau_i^+ - \Delta\tau_i^-) = -\int_{\Gamma_{i(-)}} \frac{ds}{C^2(\mathbf{r}, -)} \mathbf{v}(\mathbf{r}) \cdot \mathbf{r}'(-) \qquad [11]$$

depends only on the water velocity $\mathbf{v} \cdot \mathbf{r}'$ along the ray path. Forming sum and difference travel times separates the effects of ΔC and $\mathbf{v}$. This separation is crucial for measuring $\mathbf{v}$, because $|\mathbf{v}|$ is usually much smaller than ΔC. It is not crucial for measuring ΔC, however, and one-way, rather than sum, travel time perturbations are often used for this purpose.

The data used in the inverse problem can therefore either be the one-way travel time perturbations, e.g., $\Delta\tau_i^+$, or the sum and difference travel time perturbations, Δs_i and Δd_i. The use of one-way travel time measurements to estimate ΔC is sometimes given the special name of acoustic

thermometry, reflecting the fact that sound-speed perturbations depend mostly on temperature.

Reference States and Perturbation Models

The perturbation field ΔC and therefore the data depend on the choice of reference state, $C(\mathbf{r}, -)$. Although there is some freedom in the choice, reference states that include the range and time dependence of the sound-speed field available from ocean climatologies, for example, usually yield reference ray paths that are acceptably close to the true ones. Accurate prior estimates of the ray paths help ensure that the sampling properties of the rays are included properly in the inverse procedure and that the nonlinearities associated with ray-path mismatches are minimized.

The continuous perturbation fields ΔC and $\mathbf{v}$ are parametrized with a finite number of discrete parameters using a model. Because the tomographic inverse problem is always underdetermined, it is important to use perturbation models that are oceanographically meaningful and that provide an efficient representation of ocean variability. Separable models using a linear combination of basis functions describing the horizontal (x, y) and vertical (z) structures,

$$\Delta C(x, y, z) = \sum_{k,l,m} a_{klm} X_k(x) Y_l(y) F_m(z) \qquad [12]$$

have frequently been used for simplicity, although more general models are of course possible. The coefficients a_{klm} are the model parameters to be determined, and the X_k, Y_l, F_m are the basis functions.

Inverse Methods: Vertical Slice

The inverse problem is most simply described for the case of a single acoustic source–receiver pair. Neglecting currents and assuming that the sound-speed perturbation is a function of depth only,

$$\Delta\tau_i = -\int_{\Gamma_{i(-)}} \frac{\Delta C(z)}{C^2(\mathbf{r}, -)}\, \mathrm{d}s + \delta\tau_i, \qquad i = 1, \ldots, M \qquad [13]$$

where there are M rays. (Note that although the sound-speed perturbation has been assumed to be independent of range, the reference state can be a more general function of position.) The quantity $\delta\tau_i$ has been introduced to represent the noise contribution that is inevitably present. The noise term arises not only from observational errors but also from modeling errors associated with the representation of ΔC using a finite number of parameters and from nonlinearity errors associated with the use of the ray paths for the reference state rather than the true ray paths. (In the absence of currents the problem can be restated somewhat more simply in terms of sound slowness, $S = C^{-1}$, if desired.)

Substituting

$$\Delta C(z) = \sum_m a_m F_m(z) \qquad [14]$$

gives

$$\Delta\tau_i = \sum_m a_m \left[-\int_{\Gamma_{i(-)}} \frac{F_m(z)}{C^2(\mathbf{r}, -)}\, \mathrm{d}s \right] + \delta\tau_i, \quad i = 1, \ldots, M \qquad [15]$$

$$= \sum_m E_{im} a_m + \delta\tau_i, \qquad i = 1, \ldots, M \qquad [16]$$

The elements E_{im} depend only on prior information. This equation can be written in compact matrix notation as

$$\mathbf{y} = \mathbf{E}\mathbf{x} + \mathbf{n} \qquad [17]$$

where

$$\mathbf{y} = [\Delta\tau_i], \qquad \mathbf{E} = \{E_{im}\}, \qquad \mathbf{x} = [a_m], \qquad \mathbf{n} = [\delta\tau_i] \qquad [18]$$

The inverse problem consists (i) of finding a particular solution $\hat{\mathbf{x}}$ and (ii) of determining the uncertainty and resolution of the particular solution. Writing the estimate $\hat{\mathbf{x}}$ as a weighted linear sum of the observations,

$$\hat{\mathbf{x}} = \mathbf{B}\mathbf{y} = \mathbf{B}(\mathbf{E}\mathbf{x} + \mathbf{n}) \qquad [19]$$

For zero-mean noise, $\langle \mathbf{n} \rangle = 0$, the expected value is

$$\langle \hat{\mathbf{x}} \rangle = \mathbf{B}\mathbf{E}\langle \mathbf{x} \rangle \qquad [20]$$

The matrix $\mathbf{BE}$ is called the resolution matrix. It gives the particular solution as a weighted average of the true solution $\mathbf{x}$, with weights given by the row vectors of $\mathbf{BE}$. If the resolution matrix is the identity matrix $\mathbf{I}$, then the particular solution is the true solution. If the row vectors of $\mathbf{BE}$ are peaked on the diagonal with low values elsewhere, the particular solution is a smoothed version of the true solution. The solution uncertainty is described by the covariance matrix

$$\mathbf{P} = \langle (\hat{\mathbf{x}} - \mathbf{x})(\hat{\mathbf{x}} - \mathbf{x})^{\mathrm{T}} \rangle \qquad [21]$$

where superscript T denotes transpose.

There is an immense literature on inverse methods, and a variety of approaches are available to construct the inverse operator **B**, including least squares, singular-value decomposition (SVD), and Gauss–Markov estimation. To provide an example of one approach that has been widely used, the Gauss–Markov estimate is discussed briefly here. (The Gauss–Markov estimate is sometimes known as the 'stochastic inverse' or as 'objective mapping'.) The Gauss–Markov estimate is derived by minimizing the expected uncertainty between the true value x_j and the estimate $\hat{x}_j$, i.e., by individually minimizing the diagonal elements of the uncertainty covariance matrix **P**. The result is the Gauss–Markov theorem,

$$\mathbf{B} = \mathbf{\Phi}_{xy}\mathbf{\Phi}_{yy}^{-1} \qquad [22]$$

where

$$\mathbf{\Phi}_{xy} \equiv \langle \mathbf{x}\mathbf{y}^{\mathrm{T}} \rangle, \quad \mathbf{\Phi}_{yy} \equiv \langle \mathbf{y}\mathbf{y}^{\mathrm{T}} \rangle \qquad [23]$$

are the model–data and data–data covariance matrices, respectively. These covariances can be rewritten using $\mathbf{y} = \mathbf{E}\mathbf{x} + \mathbf{n}$. The model–data covariance matrix becomes

$$\mathbf{\Phi}_{xy} = \langle \mathbf{x}\mathbf{x}^{\mathrm{T}}\mathbf{E}^{\mathrm{T}} \rangle = \mathbf{\Phi}_{xx}\mathbf{E}^{\mathrm{T}} \qquad [24]$$

where it has been assumed that the model **x** and noise **n** are uncorrelated. The data–data covariance matrix becomes

$$\mathbf{\Phi}_{yy} = \langle (\mathbf{E}\mathbf{x} + \mathbf{n})(\mathbf{E}\mathbf{x} + \mathbf{n})^{\mathrm{T}} \rangle = \mathbf{E}\mathbf{\Phi}_{xx}\mathbf{E}^{\mathrm{T}} + \mathbf{\Phi}_{nn} \qquad [25]$$

Finally, the inverse estimate, $\hat{\mathbf{x}} = \mathbf{B}\mathbf{y}$, can be written in the familiar form

$$\hat{\mathbf{x}} = \mathbf{B}\mathbf{y} = \mathbf{\Phi}_{xx}\mathbf{E}^{\mathrm{T}}(\mathbf{E}\mathbf{\Phi}_{xx}\mathbf{E}^{\mathrm{T}} + \mathbf{\Phi}_{nn})^{-1}\mathbf{y} \qquad [26]$$

The Gauss–Markov estimator requires that the perturbation model discussed above include the *a priori* specification of the statistics of the model parameters, i.e., of the covariance matrix $\mathbf{\Phi}_{xx}$.

The solution uncertainty **P** includes contributions due to data error and due to a lack of resolution. In most realistic cases the lack of resolution dominates the solution uncertainty estimate. A key, and unfamiliar, feature of the acoustic methods is that the solution uncertainty matrix is not diagonal, i.e., the uncertainties in the model parameters are correlated in a way that depends on the ray sampling properties. These correlated uncertainties often cancel in the computation of integral properties of the solution, such as the vertically averaged heat content.

Once a solution and its uncertainty have been found, the solution must be evaluated for consistency with the various assumptions made in its construction before it can be accepted. The statistics of the residuals $(\hat{\mathbf{y}} - \mathbf{y})$, where $\hat{\mathbf{y}} = E\hat{\mathbf{x}}$, need to be examined for consistency with the assumed noise statistics $\mathbf{\Phi}_{nn}$, for example. Further, ray trajectories should be recomputed for the field

$$C(\mathbf{r}) = C(\mathbf{r}, -) + \Delta C(\mathbf{r}) \qquad [27]$$

and the resulting ray travel times compared with the original data to test for consistency. Significant differences imply that the reference state is inadequate or the model is inadequately formulated. When nonlinearities are important, iterative or other methods are needed to find a solution consistent with the original data.

The linear inverse methods used in ocean acoustic tomography are well known and widely used in a variety of fields. The crucial problem in the application to tomography is the construction of the model used to describe oceanic variability, including the choice of parametrization and the specification of the (co)variances of the model parameters and noise.

Sampling Properties of Acoustic Rays

Vertical slice: range-independent The vertical sampling properties of acoustic rays are most easily understood for the range-independent case, in which sound speed is a function of depth z only. In that case, eqn [13] can be converted to an integral over depth

$$\Delta\tau_i = -\int_{\tilde{z}^-(-)}^{\tilde{z}^+(-)} \frac{\mathrm{d}z}{C^2(z,-)\sqrt{1-(C(z,-)/\tilde{C})^2}}\,\Delta C(z) + \delta\tau_i, \qquad i = 1, \ldots, M \qquad [28]$$

using Snell's law, $C(z)/\cos(\theta) = \tilde{C}$, where θ is the ray angle relative to the horizontal and $\tilde{C}$ is the sound speed at the ray turning points $\tilde{z}^{\pm}$. The function

$$\frac{1}{C^2(z,-)\,\sqrt{1-(C(z,-)/\tilde{C})^2}} \qquad [29]$$

gives the weighting with which $\Delta C(z)$ contributes to $\Delta\tau_i$. There are (integrable) singularities in the weighting function at both the upper and lower turning point depths, where $C(\tilde{z}^{\pm}, -) = \tilde{C}$. The ray travel times are therefore most sensitive to sound-speed perturbations at the ray turning points (**Figure 3**).

The value of the weighting function is the same for depths $z^{\pm}$ above and below the sound-channel

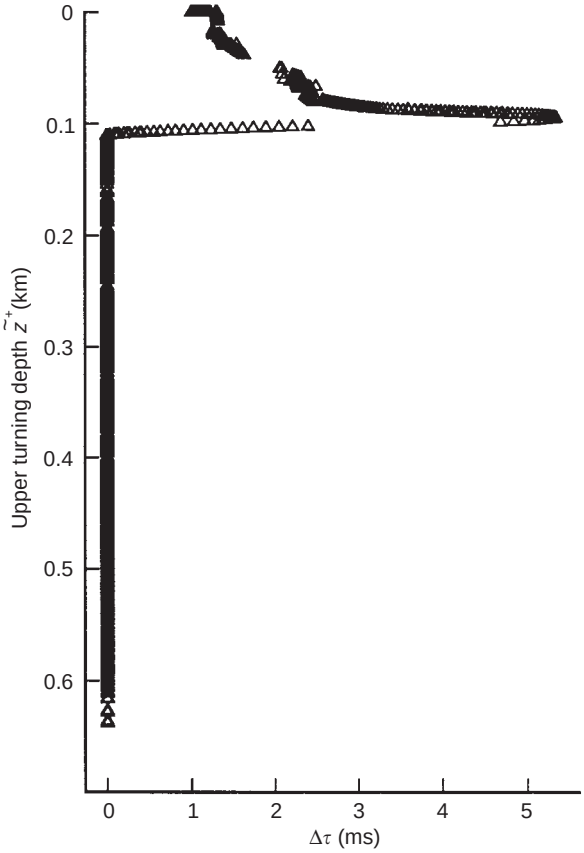

Figure 3 Travel-time perturbations computed at about 1000 km range in the North-east Pacific for a sound-speed perturbation with an amplitude of $-1\,\mathrm{m\,s^{-1}}$ at 100 m depth, linearly decreasing to zero at 90 m and 110 m. The travel-time perturbations are zero for rays with upper turning depths below 110 m, because they do not sample the perturbed region. The perturbations are sharply peaked for rays with upper turning depths between 90 m and 110 m. Rays that have upper turning depths above 90 m have nonzero perturbations because they traverse the perturbed region, but the perturbations are relatively small because the ray weighting function falls off rapidly with distance from the turning point. Adapted from Cornuelle BD, Worcester PF, Hildebrand JA *et al.* (1993) Ocean acoustic tomography at 1000-km range using wavefronts measured with a large-aperture vertical array. *Journal of Geophysical Research* 98: 16365–16377.

axis at which

$$C(z^+, -) = C(z^-, -) \qquad [30]$$

There is a fundamental up–down ambiguity for acoustic measurements in mid-latitudes. It is in principle impossible to distinguish from the acoustic data alone whether the observed travel-time perturbations are due to sound-speed perturbations located above or below the sound channel axis. This ambiguity has to be resolved from *a priori* information or from other data. This up–down ambiguity is not present in polar regions when the temperature profile is close to adiabatic, so that sound speed is a minimum at the surface and increases monotonically with depth (pressure).

Vertical slice: range-dependent A ray trapped in the sound channel, cycling between upper and lower turning points at regular intervals, samples the ocean periodically in space, so that its travel time is sensitive to some spatial frequencies but is unaffected by others. The key to understanding the horizontal sampling properties of acoustic travel times is to consider the wavenumber domain, rather than physical space, using a truncated Fourier series in x as the model for the sound-speed perturbations,

$$\Delta C(x,z) = \sum_k \sum_m a_{km} \exp\left[\frac{2\pi i}{L}(kx)\right] F_m(z),$$
$$k = 0, \pm 1, \ldots, \pm N \qquad [31]$$

The Fourier series is periodic over a domain of length L and is truncated at harmonic N. The domain is normally chosen sufficiently large (say twice the size of the source–receiver range) to avoid artifacts within the area of interest that might be caused by the periodicity.

The travel-time perturbations are then

$$\Delta\tau_i = \sum_k \sum_m a_{km} \left\{ - \int_{\Gamma_{i(-)}} \frac{\mathrm{d}s}{C^2(\mathbf{r}, -)} \times \exp\left[\frac{2\pi i}{L}(kx)\right] F_m(z) \right\} + \delta\tau_i \qquad [32]$$

where the integrals depend only on prior information. The problem has again reduced to the form $\mathbf{y} = \mathbf{E}\mathbf{x} + \mathbf{n}$, with the solution vector $\mathbf{x}$ containing an ordered set of the complex Fourier coefficients a_{km}.

The sensitivity of the travel-time inverse to various wavenumbers can be quantified by plotting the diagonal of the resolution matrix $\mathbf{BE}$ defined in eqn [20]. For the specific case of two moorings separated by 600 km, with a source and five widely-separated receivers on each mooring, the resolution matrix shows the sensitivity of tomographic measurements to the features that match the ray periodicity (i.e., have the same wavelength as the ray double loops) (**Figure 4**). Further, because the ray paths are somewhat distorted sinusoids in mid-latitudes, the resolution matrix displays sensitivity to harmonics of the basic ray double loop length. Finally, as expected, the measurements are sensitive to the mean. There are obvious spectral gaps for wavenumbers between the mean and first harmonics

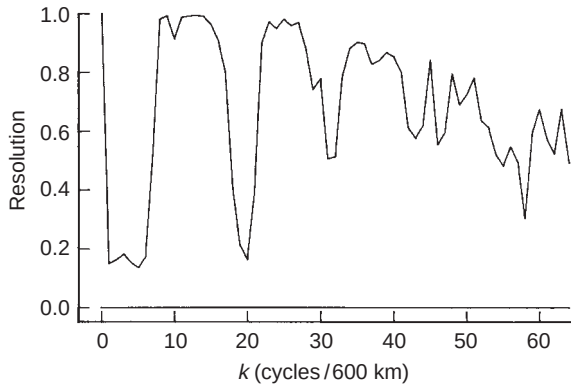

Figure 4 Diagonal elements of the resolution matrix ('transfer function') for tomographic measurements over a 600-km path in a range-dependent ocean. The plot is for the lowest baroclinic mode. Adapted from Cornuelle BD and Howe BM (1987) High spatial resolution in vertical slice ocean acoustic tomography. *Journal of Geophysical Research* 92: 11680–11692.

of the ray paths, and again between the first and second harmonics. The harmonics extend over bands of wavenumbers because the eigenrays connecting the source and receiver have a range of double-loop lengths.

Horizontal slice The sampling issues present when the goal is to map the evolving ocean using integral data are most easily understood by considering the two-dimensional horizontal slice problem. In this case sound speed is assumed to be constant in the vertical, so that ray paths travel in straight lines in the horizontal plane containing the sources and receivers. Neglecting currents,

$$\Delta\tau_i = -\int_{\Gamma_{i(-)}} \frac{\Delta C(x,y)}{C^2(x,y,-)}\,\mathrm{d}s + \delta\tau_i, \qquad i = 1, \ldots, M \qquad [33]$$

where there is one ray path per source–receiver pair and there are a total of M ray paths connecting the sources and receivers.

As was the case for the range-dependent vertical slice problem, the key to understanding the horizontal sampling properties of acoustic travel times is to consider the wavenumber domain, rather than physical space, using a truncated Fourier series in x and y as the model for the sound-speed perturbations,

$$\Delta C(x,y) = \sum_k \sum_l a_{kl} \exp\left[\frac{2\pi i}{L}(kx + ly)\right], \qquad k,l = 0, \pm 1, \ldots, \pm N \qquad [34]$$

The Fourier series is doubly periodic over the square domain of size L and is truncated at harmonic N.

The travel-time perturbations are then

$$\Delta\tau_i = \sum_k \sum_l a_{kl}\left\{-\int_{\Gamma_{i(-)}} \frac{\mathrm{d}s}{C^2(x,y,-)} \exp\left[\frac{2\pi i}{L}(kx + ly)\right]\right\} + \delta\tau_i \qquad [35]$$

where the integrals depend only on prior information. The problem has again reduced to the form $\mathbf{y} = \mathbf{E}\mathbf{x} + \mathbf{n}$, with the solution vector $\mathbf{x}$ containing an ordered set of the complex Fourier coefficients a_{kl}.

To explore the horizontal sampling properties of integral data, consider a simple scenario in which two ships start in the left and right bottom corners of a 1000-km square and steam northward in parallel, transmitting from west to east through an isotropic mesoscale field constructed to have a $1/e$ decay scale of 120 km (**Figure 5**). Inversion of the resulting travel-time data leads to an estimate that consists only of east–west contours, as all the ray paths measure only zonal averages. To interpret this result in wavenumber space, note that

$$\int_0^L \mathrm{d}x\,\Delta C(x,y) = 0 \qquad \text{for} \qquad k \neq 0 \qquad [36]$$

East–west transmissions therefore give information only on the parameters a_{0l}, which are nearly perfectly determined for the assumptions made in this simple scenario. Similarly, for north–south transmissions between two ships traveling from east to west, only the parameters a_{k0} are determined. Combining east–west and north–south transmissions determines both a_{0l} and $a_{k0,}$ but nonetheless fails to give useful maps because the majority of the wavenumbers are still undetermined. Adding scans at 45° determines wavenumbers for which $k = l$, giving improved, but still imperfect, maps.

The conclusion is that generating accurate maps from integral data requires sampling geometries with ray paths at many different angles to provide adequate resolution in wavenumber space. This requirement must be independently satisfied in any region with dimensions comparable to the ocean correlation scale. These results are a direct consequence of the projection-slice theorem.

Time-dependent Inverse Methods

The discussion of inverse methods to this point has implicitly assumed that data from a single instant in time are used to estimate the state of the ocean at that instant. Observations from different times can be combined to generate improved estimates of the

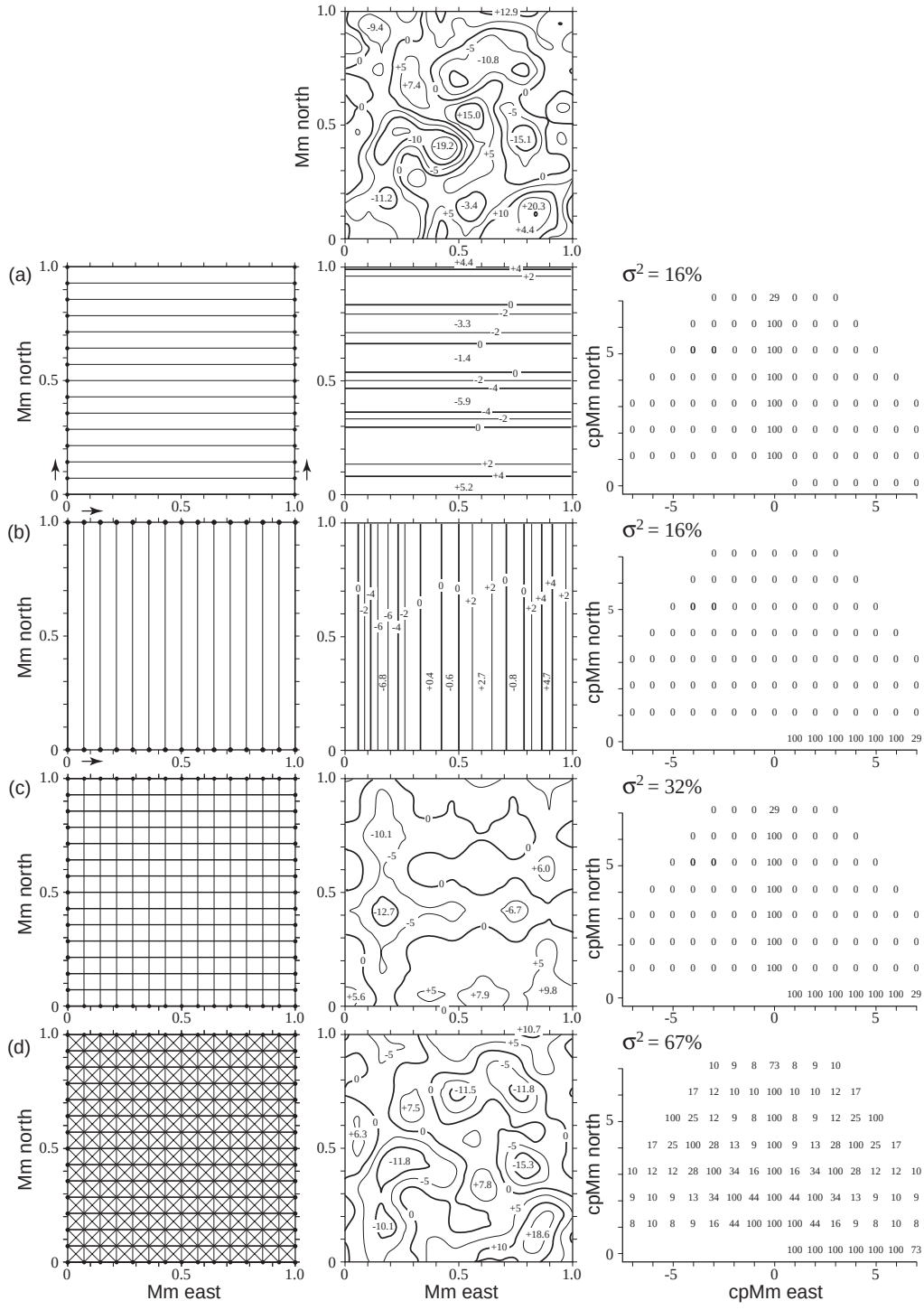

Figure 5 The top center panel is the 'true ocean,' constructed assuming a horizontally homogeneous and isotropic wavenumber spectrum, to be mapped using tomographic data. (A) W → E transmissions between two northward-traveling ships (left panel). Inversion of the travel time perturbations produces east–west contours in ΔC (middle) with only a faint relation to the 'true ocean.' Expected predicted variances in wavenumber space (right) are 0% (no skill) except for $(k, l) = (0,1),(0,2),\ldots,(0,7)$, which account for $\sigma^2 = 16\%$ of the *a priori* ΔC variance. (B) S → N transmissions between two eastward traveling ships. (C) Combined W → E and S → N transmissions, accounting for 32% of the ΔC variance. (D) Combined W → E, S → N, SW → NE, and SE → NW transmissions, accounting for 67% of the variance and giving some resemblance to the true ocean. Distances are shown in megameters (Mm) and wavenumbers are shown in cycles per megameter (cpMm). Adapted from Cornuelle BD, Munk WH and Worcester PF (1989) Ocean acoustic tomography from ships. *Journal of Geophysical Research* 94: 6232–6250.

evolving ocean, however, using a time-dependent ocean model to connect the oceanic states at those times. One seeks to minimize the misfit between the estimate $\hat{\mathbf{x}}(t)$ and the true state $\mathbf{x}(t)$ over some finite time span, instead of at a single instant.

The practice of combining data with time-evolving ocean circulation models, referred to as 'assimilation' or 'state estimation', simultaneously tests and constrains the models. A variety of approaches are available to solve this problem, including, for example, Kalman filtering and the use of adjoint methods. Although the problem of combining integral tomographic data with time-evolving models does not differ in any fundamental way from the problem of using other data types, tomographic data do differ from most other oceanographic data because their sampling and information content tend to be localized in spectral space rather than in physical space, as discussed above. It is therefore important to use methods that directly assimilate the tomographic measurements and preserve the integral information they contain. Approximate data assimilation methods optimized for measurements localized in physical space are generally inappropriate because they do not preserve the nonlocal tomographic information.

Selected Tomographic Results

Tomographic methods have been used to study a wide range of ocean processes, at diverse locations. Measurements have been made at scales ranging from a few tens of kilometers (e.g., to measure the transport through the Strait of Gibraltar) to thousands of kilometers (e.g., to measure the heat content in the north-east Pacific Ocean). This review concludes by presenting results from a few selected experiments to provide some indication of the breadth of possible applications and to illustrate the strengths and weaknesses of tomographic measurements.

Oceanic Convection

Oceanic convection to great depths occurs at only a few locations in the world (*see* **Deep Convection**). Nonetheless, it is believed to be the process by which the properties of the surface ocean and deep ocean are connected, with important consequences for the global thermohaline circulation and climate. The deep convective process is temporally intermittent and spatially compact, consisting of convective plumes with scales of about 1 km clustered in chimneys with scales of tens of kilometers. Observing the evolution of the deep convective process and quantifying the amount of deep water formed presents a difficult sampling problem. Tomographic measurements have been key components in programs to study deep convection in the Greenland Sea (1988–1989) and the Mediterranean Sea (1991–1992), as well as in an ongoing program in the Labrador Sea (1996 to present). In all of these regions the tomographic data provide the spatial coverage and temporal resolution necessary for observing the convective process.

In the Greenland Sea, for example, six acoustic transceivers were deployed from summer 1988 to summer 1989 in an array approximately 210 km in diameter (**Figure 6**), as part of the intensive field phase of the International Greenland Sea Project. The acoustic data were combined with moored thermistor data and hydrographic data to estimate the evolution of the three-dimensional temperature field $T(x, y, z)$ in the Greenland Sea during winter. (During the convective period, the hydrographic data were found to be contaminated by small-scale variability and were not useful for determining the chimney and gyre-scale structure.) A convective chimney reaching depths of about 1500 m was observed to the south west of the gyre center during March 1989. The chimney had a spatial scale of about 50 km and a timescale of about 10 days (**Figure 7**). The location of the chimney seemed to be sensitively linked to the distribution of the relatively warm, salty Arctic Intermediate Water found at intermediate depths. Potential temperature profiles extracted from the three-dimensional inverse estimates were averaged over the chimney region to show the time-evolution of the chimney (**Figure 6**). A one-dimensional vertical heat balance adequately described changes in total heat content in the chimney region from autumn 1988 until the time of chimney break-up, when horizontal advection became important and warmer waters moved into the region. The average annual deep-water production rate in the Greenland Sea for 1988–1989 was estimated from the average temperature change over the region occupied by the tomographic array to be about $0.1 \times 10^6\,\mathrm{m^3\,s^{-1}}$.

Barotropic and Baroclinic Tides

Sum and difference travel times from long-range reciprocal transmissions provide precise measurements of the sound-speed (temperature) changes associated with baroclinic (internal) tidal displacements and of barotropic tidal currents, respectively.

The availability of global sea-surface elevation data from satellite altimeter measurements has made possible the development of improved global tidal models. Tomographic measurements of tidal

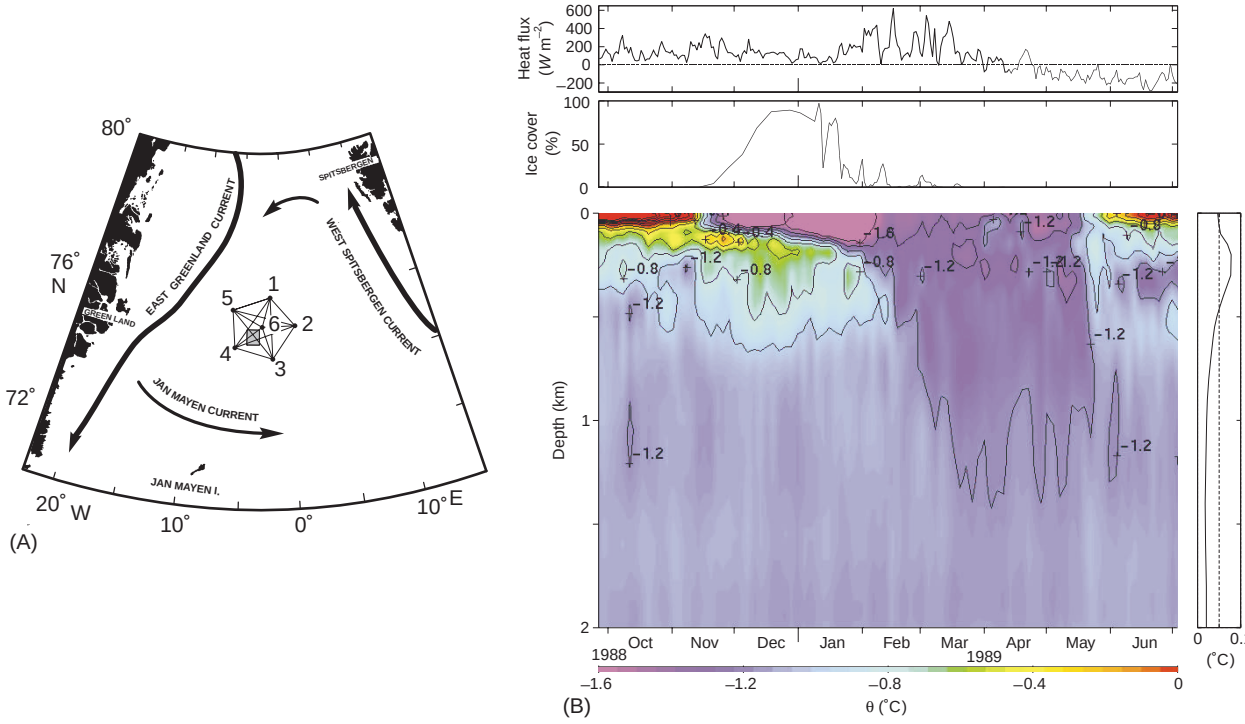

Figure 6 (A) Geometry of the tomographic transceiver array deployed in the Greenland Sea during 1988–1989. Mooring 2 failed about one month after deployment. A deep convective chimney was observed near the center of the array during March 1989 (shaded region). (B) Time-depth evolution of potential temperature averaged over the chimney region. Contour interval is 0.2°C. Typical rms uncertainty (°C) as a function of depth is shown to the right. Total heat flux (from the British Meteorological Office) and daily averaged ice cover (derived from satellite SSM/I measurements) are shown above. Adapted from Morawitz WML, Cornuelle BD and Worcester PF (1996) A case study in three-dimensional inverse methods: combining hydrographic, acoustic, and moored thermistor data in the Greenland Sea. *Journal of Atmospheric and Oceanic Techniques* 13: 659–679.

currents made in both the central North Pacific and western North Atlantic Oceans have shown that the harmonic constants for current derived from a recent global tidal model (TPXO.2) are accurate to a fraction of a millimeter per second in amplitude and a few degrees in phase in open ocean regions (**Figure 8**). Small, spatially coherent differences between the modeled and measured harmonic constants are found in the western North Atlantic near complicated topography that is unresolved in the model. These differences are almost certainly due to errors in the TPXO.2 currents. The integrating nature of the tomographic measurements suppresses short-scale internal waves and internal tides, providing tidal current measurements that are substantially more accurate than those derived from current-meter data.

Tomographic measurements of sound-speed fluctuations at tidal frequencies from the same experiments revealed large-scale internal tides that are phase-locked to the barotropic tides. Prior to these measurements it had commonly been assumed that midocean internal tides are not phase-locked to the barotropic tides (except for locally forced internal tides) and have correlation length scales of order only 100–200 km. The measurements in the North Pacific were consistent with a large-scale, phase-locked internal tide that had been generated at the Hawaiian Ridge and then propagated to the tomographic array over 2000 km to the north (**Figure 9**). These observations were subsequently confirmed from satellite altimeter data. The measurements in the western North Atlantic revealed a diurnal internal wave resonantly trapped between the shelf just north of Puerto Rico and the turning latitude for the diurnal K_1 internal tide, 1100 km distant at 30.0°N (**Figure 10**). In both cases the peak-to-peak temperature variations associated with the maximum displacement of the first baroclinic modes were only about 0.04°C. Once again, the acoustic observations of the baroclinic tide average in range and depth, suppressing internal-wave noise and providing enhanced estimates of the deterministic part of the internal-tide signal compared to measurements made at a point, such as by moored thermistors.

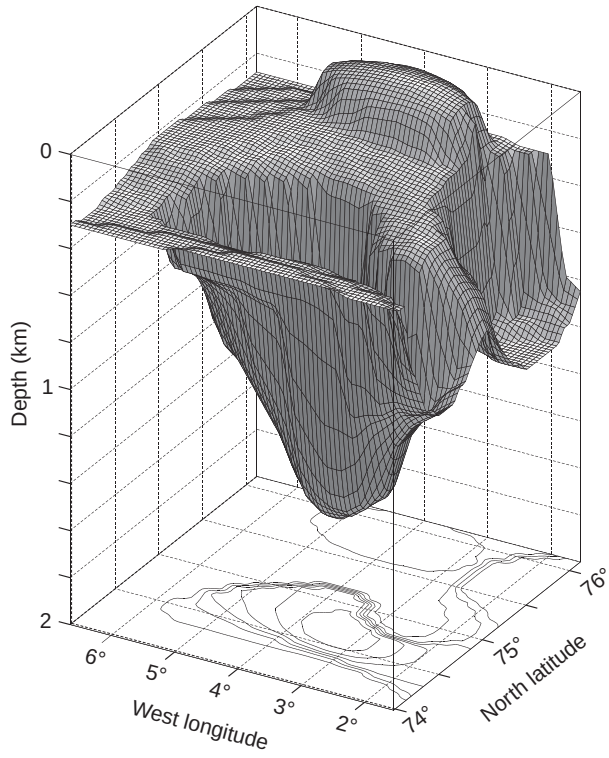

Figure 7 Mixed layer depth in the central Greenland Sea on 19 March 1989, as defined by the minimum depth of the -1.2°C isotherm. The ocean is colder than -1.2°C above this depth as a result of surface cooling and is warmer below. The main chimney reaches a maximum depth of about 1500 m in an area about 50 km in diameter centered on 74.75°N, 3.5°W, south west of the gyre center. A secondary chimney with a maximum depth of about 1000 m is evident to the north east of the gyre center, separated from the primary chimney by a ridge of warmer water. Contours of mixed layer depth are shown below. Adapted from Morawitz WML, Sutton PJ, Worcester PF *et al.* (1996) Three-dimensional observations of a deep convective chimney in the Greenland Sea during winter 1988/1989. *Journal of Physical Oceanography* 26: 2316–2343.

Heat Content

Acoustic methods have been used to measure the heat content of the ocean and its variability on basin scales, taking advantage of the integrating nature of acoustic transmissions to rapidly and repeatedly make range- and depth-averaged temperature measurements at ranges out to about 5000 km.

In the Mediterranean Sea, for example, a network of seven tomographic instruments was deployed for nine months during 1994 in the THETIS-2 experiment, including cross-basin transmissions from Europe to Africa (**Figure 11**). Although it is normally difficult to obtain heat content measurements comparable to those provided by the acoustic data, in this case one of the transmission paths was intentionally aligned with the route of a commercial ship, from which expendable bathythermograph (XBT) measurements were made at two-week intervals. The acoustic average of potential temperature between 0 and 2000 m depth over the 600-km path and the corresponding XBT average between 0 and 800 m depth agreed within the expected uncertainty of 0.03°C (**Figure 11**). Further, the evolution of the three-dimensional heat content of the western Mediterranean estimated from the acoustic data was found to be consistent with the integral of the surface heat flux provided by European Centre for Medium-range Weather Forecasts (ECMWF), after correction for the heat flux through the Straits of Gibraltar and Sicily (**Figure 11**). The acoustic data were subsequently combined with satellite altimeter data and an ocean general circulation model to generate a consistent description of the basin-scale temperature and flow fields in the western Mediterranean and their evolution over time. Acoustic and altimetric data are complementary for this purpose, with the acoustic data providing information on the ocean interior with moderate vertical resolution and the altimetric data providing detailed horizontal coverage of the ocean surface.

Similar measurements have been made in the Arctic Ocean in the Transarctic Acoustic Propagation (TAP) experiment during 1994 and in the Arctic Climate Observations using Underwater Sound (ACOUS) project beginning in 1999. During the TAP experiment, ultralow-frequency (19.6 Hz) acoustic transmissions propagated across the entire Arctic basin from a source located north of Svalbard to a receiving array located in the Beaufort Sea at a range of about 2630 km. Modal travel time measurements yielded the surprising result that the Atlantic Intermediate Water layer was about 0.4°C warmer than expected from historical data. This result was subsequently confirmed by direct measurements made from icebreakers and submarines. Acoustic data collected on a similar path during April 1999 as part of the ACOUS project indicated further warming of about 0.5°C, which was again confirmed by direct measurements made from submarines. Acoustic methods can provide the long-term, continuous observations in ice-covered regions that are difficult to obtain using other approaches.

Finally, measurements of basin-scale heat content in the Northeast Pacific were made intermittently from 1983 through 1989 using transmissions from an acoustic source located near Kaneohe, Hawaii, and more recently from 1996 through 1999 during the Acoustic Thermometry of Ocean Climate (ATOC) project using sources located off central California and north of Kauai, Hawaii. Data from

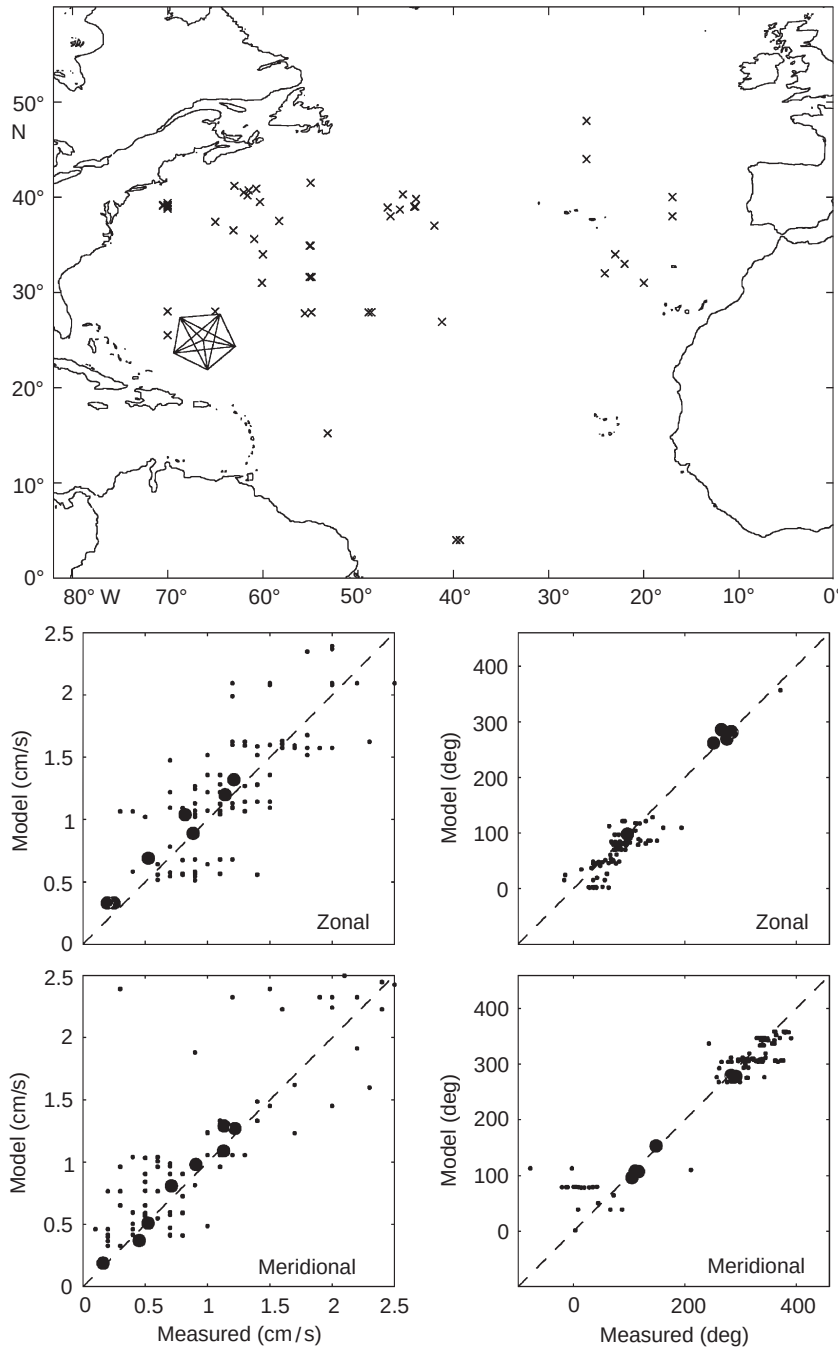

Figure 8 (Bottom) Comparison of the M_2 current harmonic constants (amplitude and phase) in the North Atlantic Ocean derived from reciprocal acoustic transmissions (filled circles) and from current meter data (dots) with those predicted by a global tidal model derived from satellite altimeter measurements (TPXO.2). (Top) The acoustic data are from the pentagonal tomographic transceiver array deployed in the western North Atlantic between Puerto Rico and Bermuda during 1991–1992. The current-meter mooring locations are indicated by crosses. Adapted from Dushaw BD, Egbert GD, Worcester PF *et al.* (1997) A TOPEX/POSEIDON global tidal model (TPXO.2) and barotropic tidal currents determined from long-range acoustic transmissions. *Progress in Oceanography* 40: 337–367.

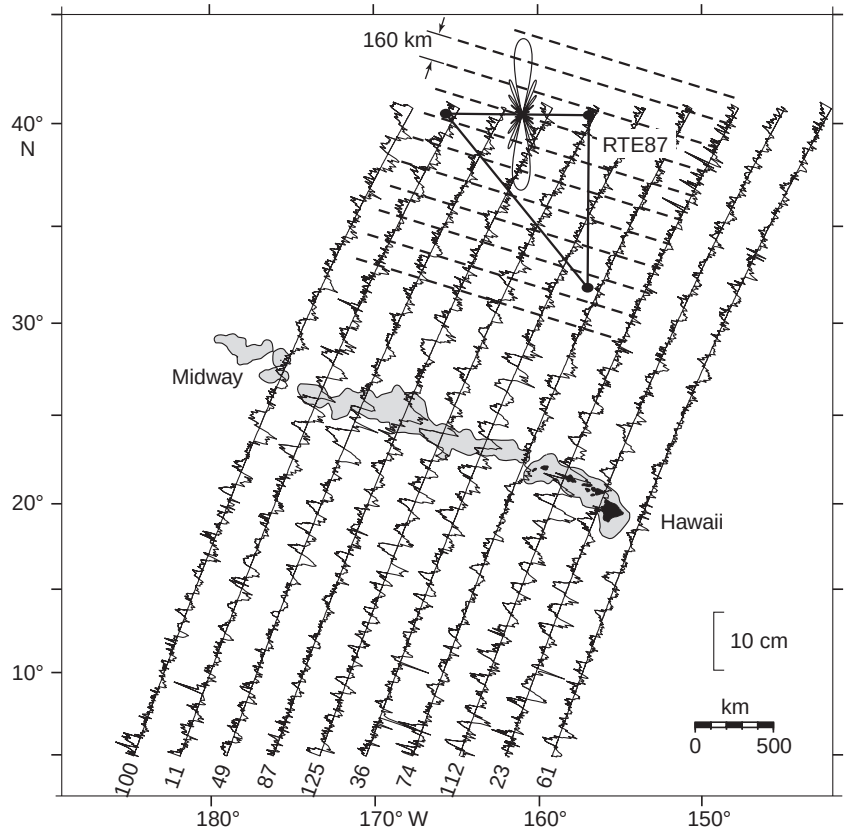

Figure 9 Schematic diagram showing the phase-locked internal tide generated at the Hawaiian Ridge and the triangular tomographic array deployed north of Hawaii during 1987 used to detect it. The dashed lines represent the crests of a wave with 160 km wavelength. Each leg of the tomographic array functions as a linear array with maximum sensitivity to an incident plane wave propagating perpendicular to the leg (i.e., with wave crests aligned parallel to the leg). The beam pattern (in dB) of the 750-km northern leg for a model-1 incident wave with a wavelength of 160 km is indicated. The satellite altimeter data that subsequently confirmed the tomographic observations are also shown. High-pass filtered M_2 surface elevations (cm) are plotted along ten ascending TOPEX/POSEIDON ground tracks. Adapted from Dushaw BD, Cornuelle BD, Worcester PF, Howe BM and Luther DS (1995) Barotropic and baroclinic tides in the central North Pacific Ocean determined from long-range reciprocal acoustic transmissions. *Journal of Physical Oceanography* 25: 631–647; Ray RD and Mitchum GT (1996) Surface manifestation of internal tides generated near Hawaii. *Geophysical Research Letters* 23: 2101–2104.

the ATOC project have shown that ray travel times may be used for acoustic thermometry at least out to ranges of about 5000 km. The estimated uncertainty in range- and depth-averaged temperature estimates made from the acoustic data at these ranges is only about 0.01°C. Comparisons between sea-surface height measurements made with a satellite altimeter and sea-surface height estimates derived using the range-averaged temperatures computed from the acoustic data indicate that thermal expansion alone is inadequate to account for all of the observed changes in sea level (**Figure 12**). Analysis of the results obtained when the acoustic and altimetric data were used to constrain an ocean general circulation model indicates that the differences result largely from a barotropic redistribution of mass, with variable salt anomalies a contributing, but smaller, factor.

Appendix: Conversion from Sound Speed to Temperature

Tomgraphic methods fundamentally provide information on the oceanic sound-speed and water-velocity fields. For most oceanographic purposes, however, temperature T and salinity Sa are of more interest than sound speed. Although sound speed C is a function of both T and Sa (as well as pressure), temperature perturbations are normally by far the most important contributor to sound-speed perturbations.

A simple nine-term equation for sound speed due to Mackenzie is

$$C(T, Sa, D) = 1448.96 + 4.591T - 5.304 \times 10^{-2}T^2 + 2.374 \times 10^{-4}T^3 + 1.340(Sa - 35)$$

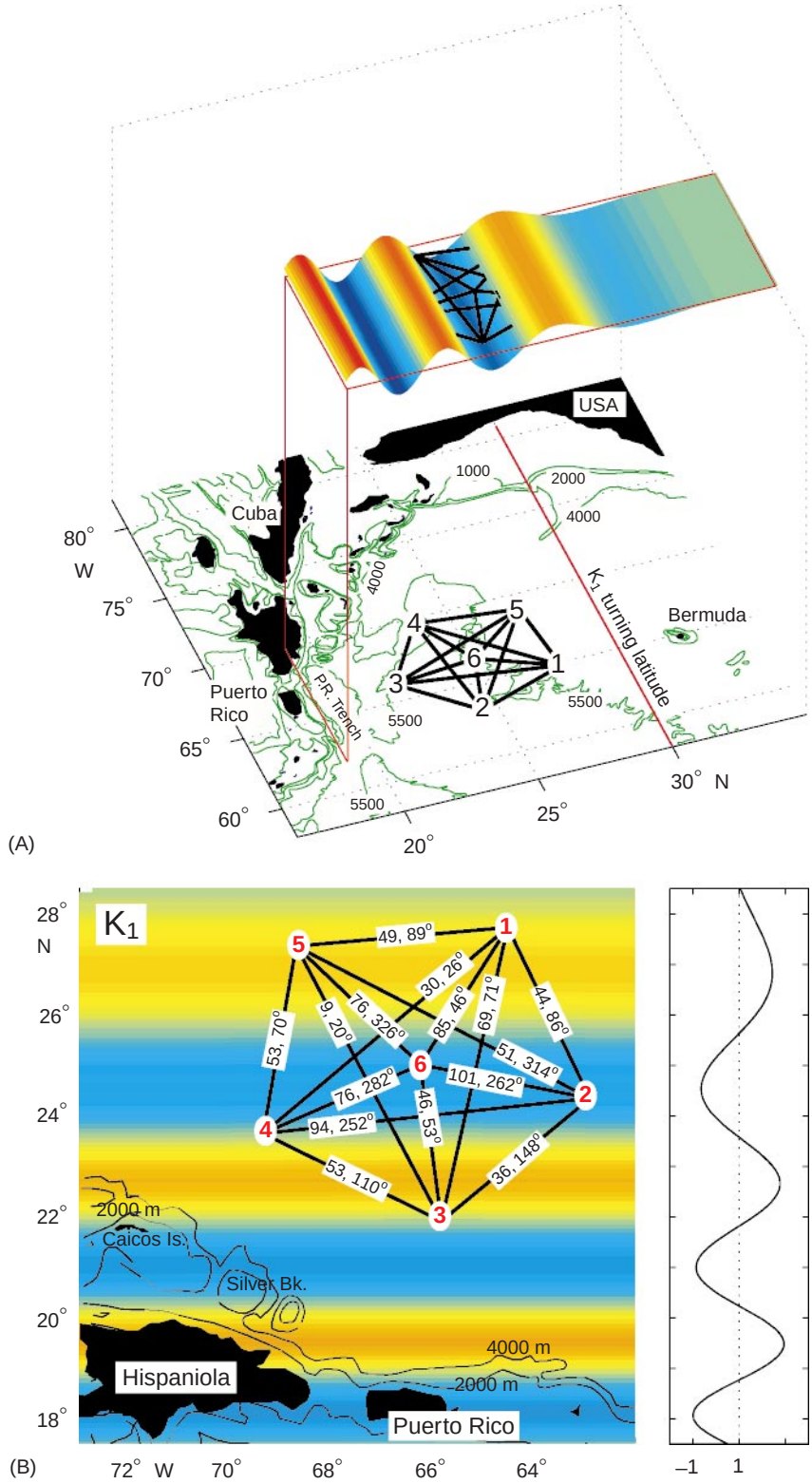

Figure 10 (A) Schematic diagram showing the predicted displacement of the lowest internal mode for the resonant diurnal (K_1) internal tide north of Puerto Rico and the six-element tomographic array deployed during 1991–1992 used to observe it. The tomographic array is about 670 km in diameter. (B) The predicted displacement of the diurnal (K_1) internal tide and the measured harmonic constants (amplitude and phase) for each acoustic path. Adapted from Dushaw BD and Worcester PF (1998) Resonant diurnal internal tides in the North Atlantic. *Geophysical Research Letters* 25: 2189–2192.

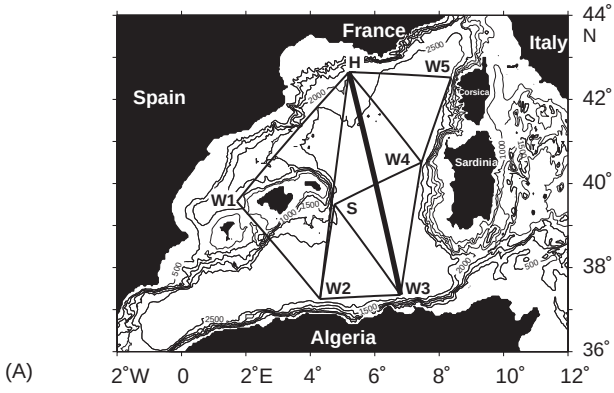

(A)

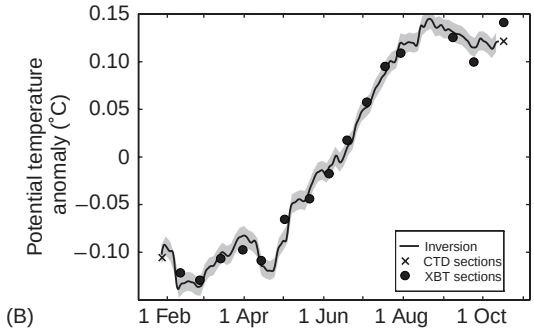

(B)

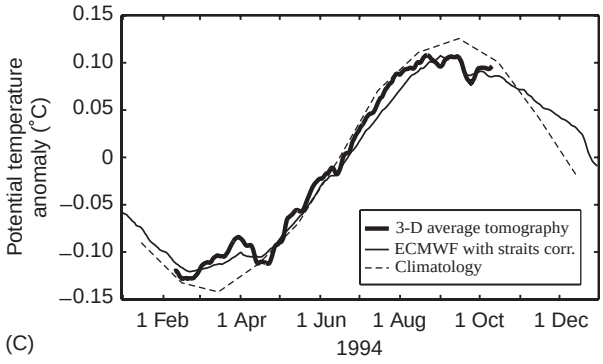

(C)

Figure 11 (A) Geometry of the THETIS-2 experiment in the western Mediterranean Sea, showing the instrument locations and acoustic transmission paths. The transmission path from source H to receiver W3 (heavy solid) coincided with an XBT section occupied every two weeks. (B) Range- and depth-averaged potential temperature (relative to 13.111°C) over 0–2000 m depth and over the 600 km path from source H to receiver W3 derived from the acoustic data, from CTD data, and from XBT data. The shaded band indicates the uncertainty in the temperature estimates derived from the acoustic data. (C) Evolution of the three-dimensional average heat content for the western Mediterranean during 1994 derived from the acoustic data, from the ECMWF surface heat fluxes corrected for heat transport through the Straits of Gibraltar and Sicily, and from climatology. Adapted from Send U, Krahmann G, Mauuary D *et al.* (1997) Acoustic observations of heat content across the Mediterranean Sea. *Nature* 385: 615–617.

$$+ 1.630 \times 10^{-2} D + 1.675 \times 10^{-7} D^2 - 1.025 \times 10^{-2} T(Sa - 35) - 7.139 \times 10^{-13} T D^3 \quad [37]$$

where C is in ms^{-1}, T is in degrees Celsius, Sa is in parts per thousand (ppt), and D is the depth (positive down) in meters. Differentiating,

$$\frac{\partial C}{\partial T} = 4.59 - 0.106T + 7.12 \times 10^{-4} T^2 - 1.03 \times 10^{-2}(Sa - 35) \quad [38]$$

$$\frac{\partial C}{\partial Sa} = 1.34 - 1.03 \times 10^{-2} T \quad [39]$$

where a slight depth dependence has been dropped. The derivative $\partial T/\partial C = 1/(\partial C/\partial T)$ varies significantly with temperature (**Figure 13**).

To first order, the fractional change in sound speed is then

$$\Delta C/C = \alpha \Delta T + \beta \Delta Sa \quad [40]$$

where

$$\alpha = \frac{1}{C}\frac{\partial C}{\partial T} \approx 2.4 \times 10^{-3} (^\circ\mathrm{C})^{-1} \quad [41]$$

$$\beta = \frac{1}{C}\frac{\partial C}{\partial Sa} \approx 0.8 \times 10^{-3} (\mathrm{ppt})^{-1} \quad [42]$$

at 10°C. For a locally linear temperature–salinity relation,

$$Sa = Sa(T(-)) + \mu \Delta T \quad [43]$$

where $T(-)$ is the reference temperature profile corresponding to the reference sound-speed profile $C(-)$ and $\Delta T = T - T(-)$. The fractional change in sound speed is then

$$\Delta C/C = \alpha \Delta T(1 + \mu\beta/\alpha) \quad [44]$$

In midlatitudes a typical value for μ might be $0.1(\mathrm{ppt})(^\circ\mathrm{C})^{-1}$, giving $\mu\beta/\alpha \approx 0.03$. Thus the sound-speed perturbation ΔC depends to first order only on the temperature perturbation ΔT.

The sound-speed perturbation profile $\Delta C(z)$ derived from the acoustic data can be easily converted to the corresponding temperature perturbation profile

$$\Delta T(z) = \int_{C(-)}^{C(-)+\Delta C} \frac{\partial T}{\partial C}\, \mathrm{d}C, \quad [45]$$

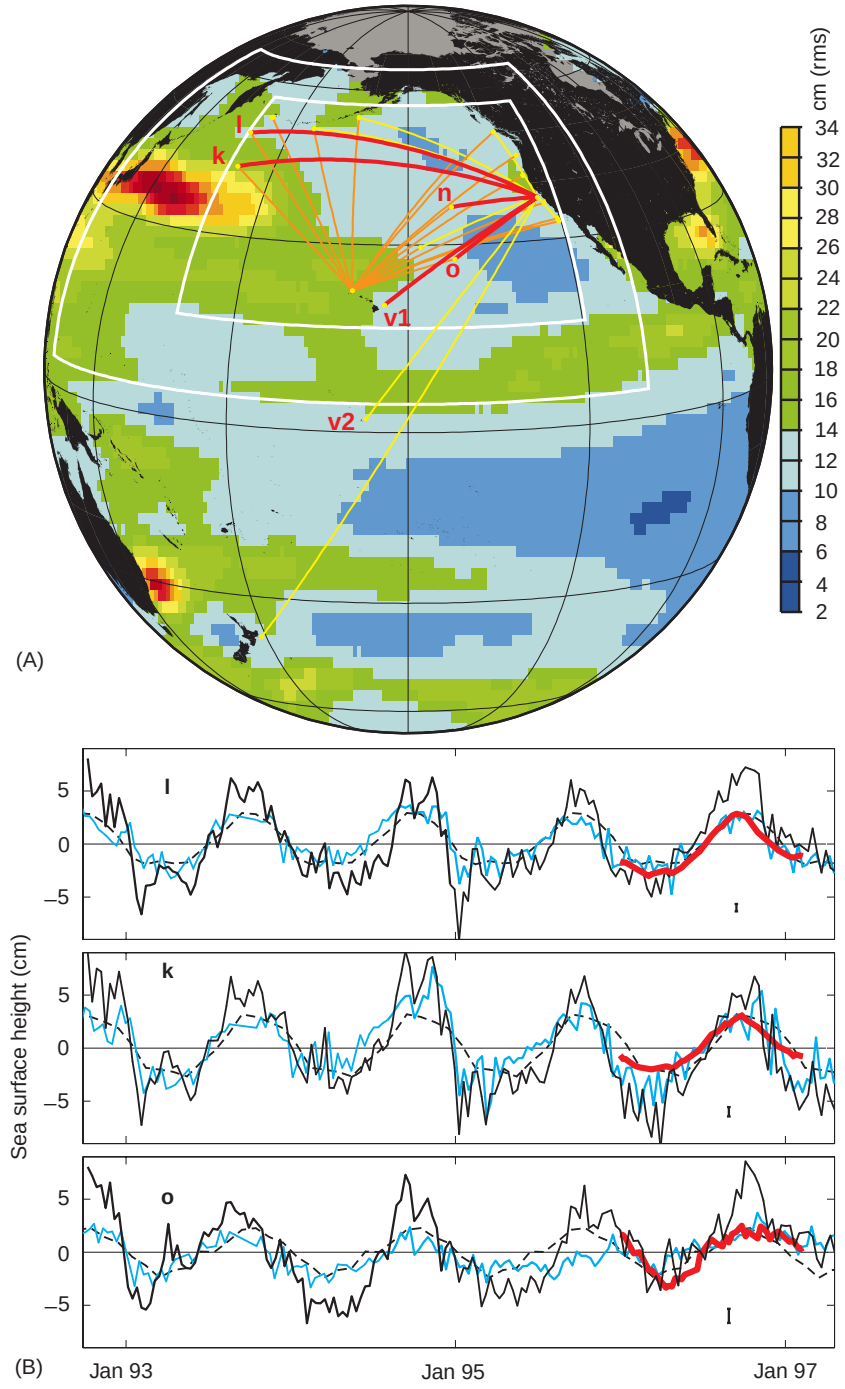

Figure 12 (A) The ATOC acoustic array is superimposed on a map of the root-mean-square (rms) sea level anomaly from altimetric measurements. Transmission paths from sources off central California and north of Kauai to a variety of receivers are shown. (B) The range-averaged sea-surface height anomaly along several of the acoustic sections from satellite altimeter data (solid black), inferred from the acoustic data (solid red), computed from climatological temperature fluctuations (dashed), and derived from an ocean general circulation model (solid blue). Uncertainties are indicated for the acoustic estimates. Adapted from ATOC Consortium (1998) Ocean climate change: comparison of acoustic tomography, satellite altimetry, and modeling. *Science* 281: 1327–1332.

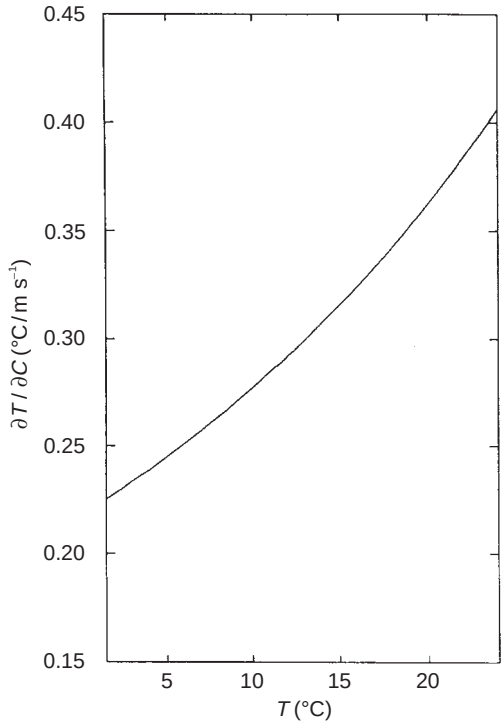

Figure 13 The derivative $\partial T/\partial C$ as a function of temperature. Adapted from Dushaw BD, Worcester PF, Cornuelle BD and Howe BM (1993) Variability of heat content in the central North-Pacific in summer 1987 determined from long-range acoustic transmissions. *Journal of Physical Oceanography* 23: 2650–2666.

where the integral allows for the dependence of $\partial T/\partial C$ on temperature.

See also

Acoustics, Arctic. Acoustics in Marine Sediments. Deep Convection. Internal Tides. Inverse Models. Tides.

Further Reading

Khil'ko AI, Caruthers JW and Sidorovskaia NA (1998) *Ocean Acoustic Tomography: A Review with Emphasis on the Russian Approach*. Nizhny Novgorod: Institute of Applied Physics, Russian Academy of Sciences.

Munk W, Worcester P and Wunsch C (1995) *Ocean Acoustic Tomography*. Cambridge: Cambridge University Press. (The review given here draws heavily from, and uses the same notation as, this monograph, which provides a comprehensive account of the elements of oceanography, acoustics, signal processing, and inverse methods necessary to understand the application of tomographic methods to studying the ocean.)

Munk W and Wunsch C (1979) Ocean acoustic tomography: a scheme for large scale monitoring. *Deep-Sea Research* 26: 123–161.

Worcester PF (1977) Reciprocal acoustic transmission in a mid-ocean environment. *Journal of the Acoustical Society of America* 62: 895–905.

TOPOGRAPHIC EDDIES

J. H. Middleton, The University of New South Wales, Sydney, New South Wales, Australia

doi:10.1006/rwos.2001.0145

Introduction

Topographic eddies in the ocean may have a range of scales, and arise from flow separation caused by an abrupt change in topography. This abrupt change may be of large scale, such as a major headland, in which case the topographic eddy is essentially a horizontal eddy of scale many tens of kilometers in a shallow coastal ocean. Eddies also occur at much smaller scales when ocean currents flow around small reefs, or over a rocky seabed. In this case the topographic eddies are perhaps only meters or centimeters in scale. A rule of thumb is that topographic eddies are generated at the same length scales as the generating topography.

Perhaps the earliest recorded evidence of a topographic eddy in the ocean comes from Greek mythology, where there is mention of a whirlpool occurring beyond the straits of Messina, between Sicily and Italy. Jason and the Argonauts in their vessel the Argo had to find the path between the Cliff known as Scylla, and the whirlpool having the monster Charybdis. The whirlpool still exists and occurs as the tides flood and ebb through the narrow straits. Another well-known tidal whirlpool, intensified at times by contrary winds and often responsible for the destruction of small craft, occurs off the Lofoten Islands of Norway. The Norwegian word maelstrom is associated with the whirlpool.

More recently, the fishing and marine lore of the Palau District of Micronesia, and the knowledge of ocean currents held apparently for hundreds, if not thousands, of years has been investigated. In fact, it was found 'The islanders had discovered stable vortex pairs and used them in their fishing and navigation long before they were known to science.'